PHOTON ARRAY FOR STUDIES WITH RADIOACTIVE ION AND STABLE BEAMS

Report 1 on the PARIS Calorimeter Simulations

IPN Lyon, 69622 Villeurbanne, France
June 2007

Abstract

This report summarises some of the preparatory simulations for the PARIS calorimeter. The scheme of the simulations is presented and the results are commented. These first studies based on absorption probability, energy deposit pattern, angular spread, longitudinal and radial expansion of the shower generated by incident photons over a wide range of energy suggest the relevance of a two-shell configuration. Further investigations aimed to define more precisely the most suited design are presented and guide lines for the forthcoming simulations are given.

1. Simulation details

The simulations are performed with the GEANT4 package, and the data analysis is done with ROOT.

1.1 Geometry

A simple geometry of either a single or concentric shells (spherical layers) consisting of various materials, inner/outer radii and initial/final ϑ and ϕ angles is considered. So far, we assume *un-segmented* layers. Crystal encapsulation, envelopes, support or any other structural piece are *not* included yet. An illustrative picture of some of the geometries handled in this document is presented in Fig. 1. Several materials are defined in the available package (LaBr3, CsI, NaI, BGO, BaF2, …). Air shall be taken for the medium (e.g. between 2 layers). **Although the present document mostly concentrates on a two-shell configuration, alternative options shall not be neglected** and will be considered as well in near future (see section 4).

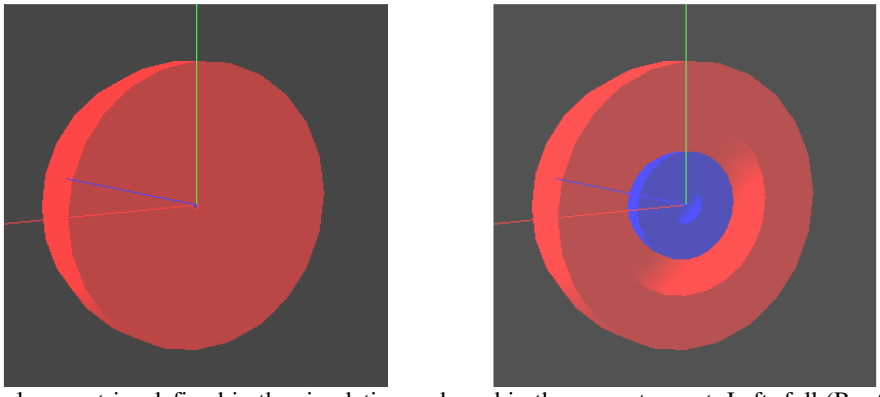

Fig. 1: Typical geometries defined in the simulation and used in the present report. Left: full (R_{in}=0cm) sphere. Right: arrangement of 2 concentric shells.

1.2 Physics process

In the present report, all simulations have been done with the standard electromagnetic physics processes list of GEANT4 which should be well suited for the energy domain the PARIS collaboration is concerned with. The cut-off parameter is set here at 0.1mm for all particles (γ, e^- and e^+) (the default value is 1mm). In GEANT4, this threshold above which no secondaries are generated is introduced in order to avoid infrared divergence. The cut-off is defined in terms of range. I.e. for a cut-off of 0.1mm, depending on the material, the threshold in energy is around 130-190 keV for e^-/e^+ and 7-20keV for photons. Although the secondary particles below the threshold are not generated (no track computed), the energy carried away by them is known. Once the threshold is reached, the remaining amount of energy is deposited in the medium. In principle, the cut-off parameter taken in the simulation shall be comparable to the size of the detection pixel. The effect of using other physics process lists (namely, the so called Low-Energy and Penelope lists dedicated to very low energies) as well as the effect of the cut-off parameter have been investigated: their influence on the extent and energy deposit pattern of the shower generated by the incident photon has been found negligible.
Note that *only physics interactions are considered* presently. Light collection, noise and threshold considerations are *not* included in the simulation yet.

1.3 Generator

The generator considered in this report consists of isotropically emitted γ rays which energy is either uniformly distributed over a wide range up to 40 MeV or consists of a cascade of discrete lines (from 100keV up to 30MeV). The secondary particles are γ rays, electrons and positrons. The possibility of shooting particles in a restricted angular range is available as well via the generator input file of the package. In addition, the influence of the boost experience by the γ's due to a potentially moving source can be ordered in the input file. Along the present report, we restrict to emitters at rest.

2. Results

As a starting point, a set of "global/bulk" quantities are defined and their distributions are drawn for a few detector configurations. The main goal of the present report being qualitative, unless specifically indicated, we restrict here to complete shells i.e. a 4π-angular coverage. In future, simulations will be done with a configuration accounting, at least, including the finite aperture mandatory for the beam.

2.1 Full absorption

2.1.a. Single full shell configuration

Let us call E_{inc} and E_{det} the true energy of the incident γ ray and the amount of energy deposited in the detector, respectively. We then define *full absorption* as the probability of the incident γ for depositing its whole amount of energy (i.e. $E_{det} > 99\%E_{inc}$) in the detector. This probability is shown in Fig.2 as a function of the γ-ray energy for a 20cm thick full shell (R_{in}=0cm and R_{out}=20cm) for various materials. Note the specific significance of this quantity: It does not account for events in which e.g. 80 or 90% of the energy is deposited,

although such events might not be as worse neither. That has to be kept in mind when drawing conclusions from full absorption curves.
It is observed that BGO is most efficient : Even for very high-energy γ-rays, the probability for full absorption exceeds 90%, whereas it drops to 50% for NaI at 25MeV. The probability of full absorption directly reflects the density of the material.

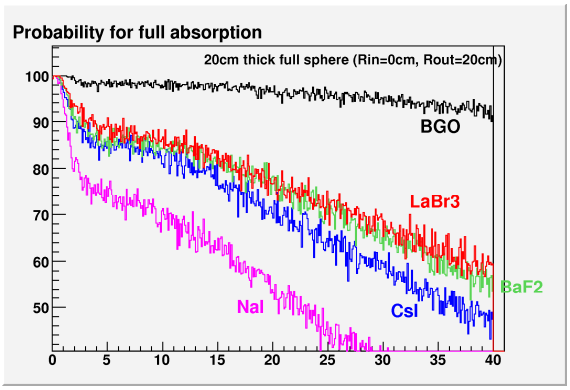

Fig. 2: Probability for full absorption as a function of the incident γ-ray energy E_{inc} for a 20cm thick full spherical layer made of various materials.

2.1.b. Concentric two-shell configuration

Instead of a single full shell, we consider in Fig.3 an arrangement of 2 concentric shells with various materials, inner and outer radii. Since LaBr3 and CsI have similar densities, the full absorption curve for a 5cm thick LaBr3 layer followed by a 15cm thick CsI layer resembles the result obtained in Fig.2 for 20cm of either LaBr3 or CsI. One notices that a 5cm LaBr3 + 15cm CsI configuration is rather efficient up to high γ-ray energies. BGO for the outer shell would, of course, be better. Yet, the very poor energy resolution and low light-yield inherent to BGO do not match the requirements of the PARIS physics cases.
Although the remainder of the present document is restricted to a 4π geometry, we show in the bottom row of Fig.3 the influence of a finite aperture mandatory for the beam pipe. Conical holes of various sizes have been considered. The corresponding angular coverage is reported in Table 1 for the displayed examples.

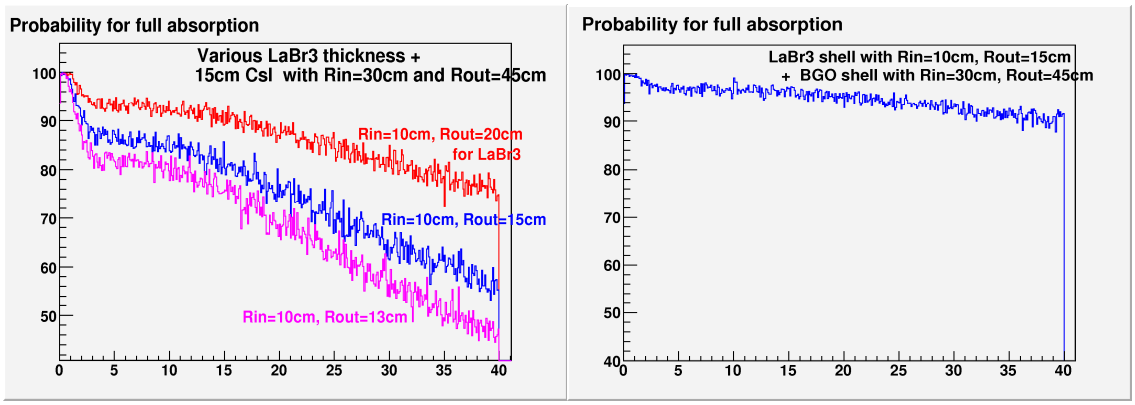

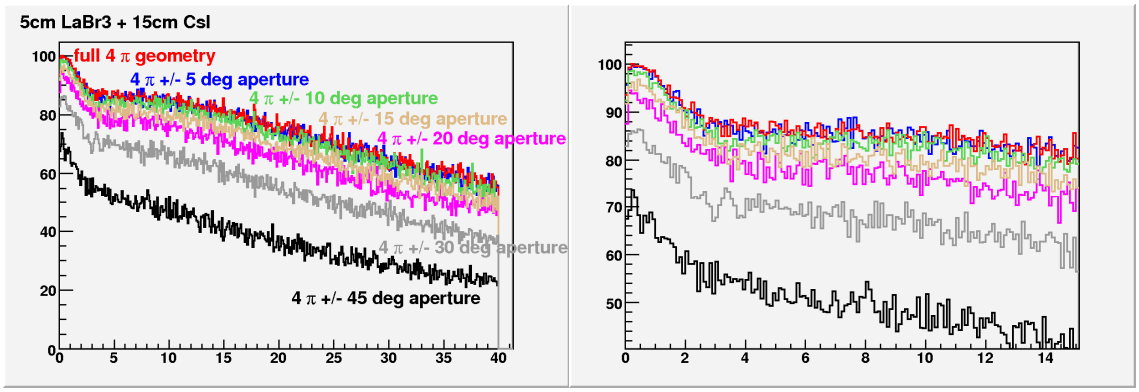

Fig. 3: Left top panel: Probability for full absorption as a function of the incident γ energy for a LaBr3 layer with R_{in}=10cm and R_{out}=15cm, 20cm, 25cm followed by a CsI layer with R_{in}=30cm and R_{out}=45cm. Right top panel: Probability for full absorption as a function of E_{inc} for a LaBr3 layer with Rin=10cm and Rout=15cm followed by a BGO layer with R_{in}=30cm and R_{out}=45cm. Left bottom panel: Probability for full absorption as a function of E_{inc} for a LaBr3 layer with R_{in}=10cm and R_{out}=15cm followed by a CsI layer with R_{in}=30cm and R_{out}=45cm for a perfect 4π-geometry and when including forward and backward conical holes of various apertures (from ±5° up to ±45° around the beam axis). Right bottom panel: Identical to the left panel with a zoom in the region $E_\gamma \in$ [0-15] MeV.

	Ω (msr)	**% of coverage**
$\vartheta_0 = 5°$	48	0.4
$\vartheta_0 = 10°$	190	1.6
$\vartheta_0 = 15°$	428	3.4
$\vartheta_0 = 20°$	758	6.0
$\vartheta_0 = 30°$	1684	13.4
$\vartheta_0 = 45°$	3680	29.2

Table 1: Angular coverage (in msr and % of $4\cdot\pi$) for a spherical geometry with various finite forward and backward conical apertures. NB: The opening angle subtended by a conical symmetric hole characterized by $\vartheta \in [-\vartheta_0,+\vartheta_0]$ is given by: $\Omega = 2\cdot\pi(1 - cos\vartheta_0)$.

2.2 Energy deposit pattern: collection and loss

Even with thick layers, part of the energy is lost outside the detector bulk. In addition to the aforementioned influence of the density of the material preventing from full absorption, the partial collection of the incident energy can also be due to the escape of the photon(s) resulting from positron annihilation after pair creation by the incident γ. To illustrate this, Fig. 4 and 5 show the distribution of the total energy deposited inside the detector bulk for a few incident γ-ray energies E_{inc} (recognized by their photo-peaks). A single full shell configuration is considered in Fig.4 and a two-shell ensemble in Fig. 5. In the latter case, in addition to the deposit in the whole ensemble, the energy deposited in each individual layer is shown.
With increasing E_{inc}, the probability for photo-electric effect decreases in the inner shell and increases in the outer shell. Above about 5MeV, pair creation dominates as compared to Compton scattering and photoelectric effect. When taking place near the outer edge surface of the detector (or of a given shell in case of several layers), the probability for the annihilation photon(s) to escape the detector (or the given shell) increases. For a two-shell configuration, that leads to the appearance of peaks at (E_{inc}-511) and (E_{inc}-1022) keV in the energy deposit distribution of the layer under consideration, and to a peak at 511keV in the counterpart shell

(see Fig. 5 and 6). The potential 1022keV escape channel is probably by far too weak (see discussion below). Of course, no escape peak at 511 keV is present for the single full shell of Fig. 4. The comparison of the energy deposit distributions in the whole detector, inner and outer shells further illustrates the diffusion of annihilation photon(s) from one shell to the other, as shown on the zoom of Fig.5 in the left panel of Fig.6. Setting a gate at 511 keV for the energy deposit in the inner (outer) shell clearly evidences the (E_{inc}-511) keV counterpart peak in the outer (inner) shell (see right panel of Fig. 6).

For a reasonably thick detector, the probability of escape and loss of the annihilation photon(s) remains small (about 2 orders of magnitude weaker than the corresponding photo-peak in the top left corner of Fig.5). The ratio ($I_{511\ escape}/I_{photo}$) of the intensity of the (E_{inc}-511keV) escape peak to that of the photo-peak is larger in the inner than in the outer shell. Together with the nearly identical number of counts in the full and dashed peaks in the left panel of Fig.6, this observation suggests a quite small probability for *retro*-diffusion from the outer to the inner layer .

The evolution of the ($I_{511\ escape}/I_{photo}$) ratio with incident γ-ray energy is puzzling. For E_{inc}=2-8 MeV, Compton scattering and pair creation fairly compete; the former steeply decreases while the latter steeply increases. The intensity of the (E_{inc}-511) keV peak below E_{inc}=10MeV thus critically depends on the relative percentage of events carried away by Compton interactions as compared to pair creations. At the high-energy limit for the Compton scattering, the extent of the corresponding shower can be such as full absorption decreases. At the same time, in this intermediate energy domain, the shower generated by pair creation can start rather close to the inner surface of a given shell. Indeed, for this E_{inc} range, the mean free path of pair conversion is smaller than for Compton scattering. Consequently, for pair creation events, full absorption is quite probable. At incident energies above 10MeV, pair creation enters into play only. The corresponding mean free path *slightly decreases* with increasing E_{inc}. Yet, the energy of the secondary particles created by the incident photon increases and the shower may considerably extend. In addition, secondary photons created by Bremsstrahlung of energetic charged particles can undergo pair creation as well. The annihilation photon(s) stemming from such secondary pair conversion might – or not – escape the detector depending on where the positron annihilates. All these considerations result in a complex interplay for the energy deposit pattern. Investigations are under progress to deepen this point. Some useful cross section and mean free path values are given in Appendix A.

In Fig. 5, peaks at (E_{inc}-1022)keV related to the escape of two annihilation photons are present for E_{inc}=30MeV and 40MeV, only. According to the aforementioned decreasing mean free path for pair conversion with increasing E_{inc}, the *first* annihilation process might occur closer to the outer surface of the inner shell for E_{inc}=10-20MeV than for E_{inc}=30-40MeV, leading to a greater probability for the escape of both annihilation photons. That is not observed. Nonetheless, it should be noted that the number of interactions in the shower is larger at 40MeV than at 20MeV, what increases the probability of numerous secondary pair creations more and more closer to the outer surface, and thus the escape of two annihilation photons. At the same time, in Fig.5 and 6, the thickness of the inner shell is typically in the range of the involved mean free paths, what certainly affects the clarity of the picture. In Fig. 6a, considering a smaller thickness brings to light escape of two annihilation particles at lower E_{inc}, while for thicker inner layers such double escape is inexistent up to the highest energies, the probability for re-absorbing the secondary particles being larger.

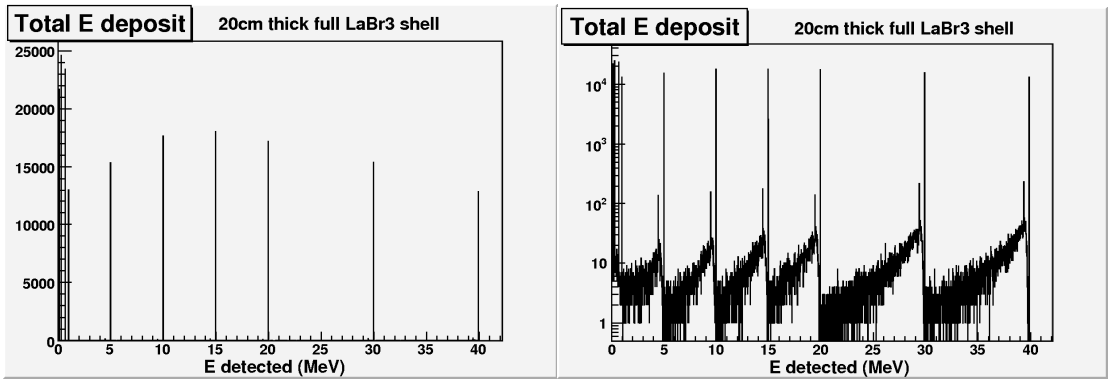

Fig. 4: Amount of energy deposited in the detector bulk for a single full 20cm thick LaBr3 sphere in linear (left) and logarithmic (right) scale. Discrete incident γ-ray energies of E_{inc}=100, 300, 700 keV, 1, 5, 10, 15, 20, 30, 40MeV are considered.

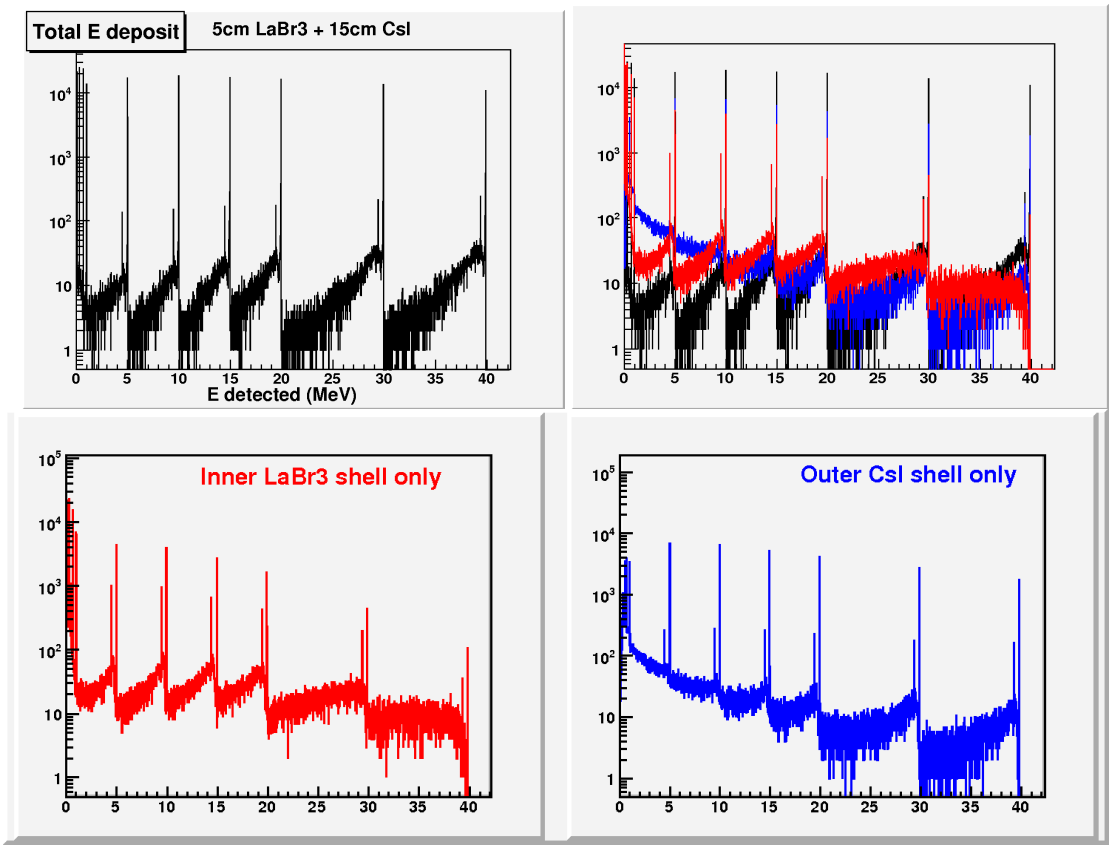

Fig. 5: Amount of energy deposited in the detector bulk for a two-shell configuration of a 5cm thick LaBr3 layer combined with a 15cm thick CsI layer. Discrete incident energies of E_{inc}=100, 300, 700 keV, 1, 5, 10, 15, 20, 30, 40MeV are considered. The black histogram refers to the deposit in the ensemble of the 2 shells, while the red (blue) curve corresponds to the deposit in the inner (outer) layer only.

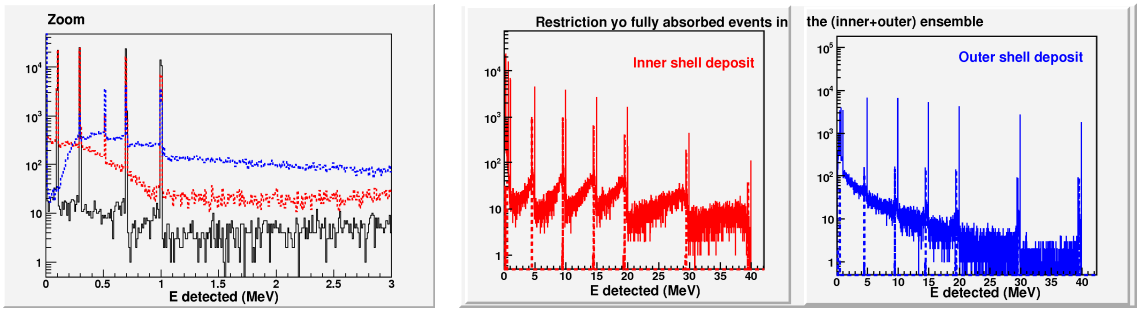

Fig. 6: Left panel: Zoom in the low-energy region of the right-bottom panel of Fig. 5. Right panel: Energy deposit in the two layers are shown individually as in Fig.5 restricting to events which are fully absorbed in the detector (either in one of the 2 shells or with a partition of the energy deposit in the 2 shells). The dashed spectra refer to those events in coincidence with a 511 keV peak in the counterpart shell of the one under consideration.

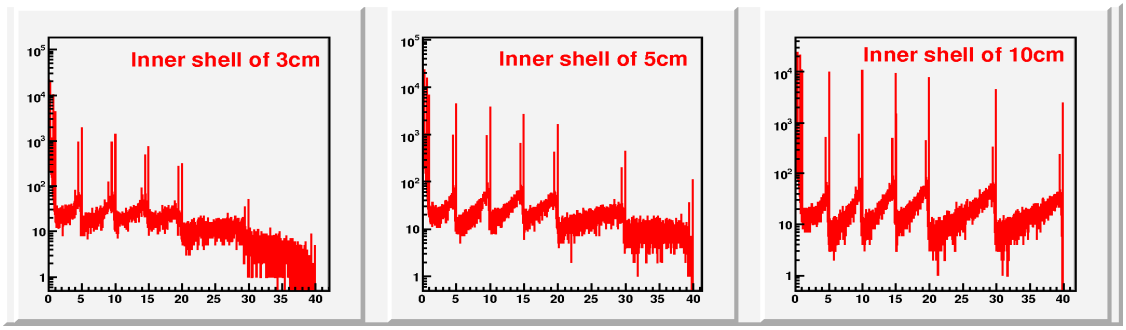

Fig. 6a: Amount of energy deposited in the inner shell as in Fig.5 and 6 but for various thickness of the inner LaBr3 layer as indicated. Of importance here are the relative intensity of the photo-, 511KeV single- and double-escape peaks as function of E_{inc} and inner thickness.

Some useful numerical values for the absorption probability are given in Tables 2 and 3 for a 20cm thick LaBr3 full sphere and the two-shell (5cm LaBr3 + 15cm CsI) arrangement, respectively. For both configurations, the probability of detecting 97% of the incident E_{inc} is rather large, even for the highest E_{inc}. At the same time, the probability for losing more than 10% of E_{inc} outside the detector bulk remains small. Hence, **a total thickness of 20cm seems rather well suited, ensuring the collection of the major part of the incident energy in the PARIS domain**. This preliminary conclusion might, nonetheless, be further studied along the determination of the reconstruction algorithm (including both the add-back procedure enabling to recover the true initial energy and the position/angular resolution). The rather sudden increase of the percentage of events depositing less than 90% of E_{inc} inside the detector bulk from E_{inc}=1 to 5MeV is partly assigned to the onset of fair competition between Compton scattering and pair creation. Also, the larger scattering inherent to the Compton process with increasing E_{inc} affect the energy deposit (see above and sections 2.5 and 2.6). Nonetheless, it is worth noting that the maximum for the probability of missing more than 10% of E_{inc} that appears around 4-6MeV is partly of numerical origin connected to the fact that the escape of one single annihilation photon already carries away more than, or almost, 10% of E_{inc}. Once this numerical bias disappears, the probability for losing more than 10% of E_{inc} very slightly increases. This weak increase might result from the complex interplay mentioned earlier.

Incident γ energy E_{inc}	**% of events which are fully absorbed**	**% of events for which less of 3% of E_{inc} is lost**	**% of events for which more than 10% of E_{inc} is**

		(i.e. more than 97% is absorbed)	lost (i.e. less than 90% is absorbed)
1MeV	**98.5**	**98.5**	**1.5**
2MeV	**93.1**	**93.1**	**6.9**
3MeV	**90.17**	**90.18**	**9.7**
4MeV	**88.13**	**88.14**	**11.05**
5MeV	**87.79**	**87.80**	**10.7**
5.3MeV	**87.33**	**87.4**	**10.4**
10MeV	**86.0**	**86.5**	**9.1**
20MeV	**77.5**	**81.8**	**9.8**
30MeV	**65.1**	**75.4**	**11.5**
40MeV	**58.7**	**70.7**	**12.4**

Table 3: Information about the absorption pattern for a 20cm thick LaBr3 shell.

Incident γ energy E_{inc}	% of events which are fully absorbed	% of events for which less of 3% of E_{inc} is lost (i.e. more than 97% is absorbed)	% of events for which more than 10% of E_{inc} is lost (i.e. less than 90% is absorbed)
1MeV	**97.6**	**97.7**	**2.1**
5MeV	**86.2**	**86.7**	**11.8**
10MeV	**84.8**	**85.8**	**10.3**
20MeV	**75.7**	**79.8**	**11.1**
30MeV	**65.1**	**73.0**	**12.6**
40MeV	**55.7**	**67.5**	**14.1**

Table 3: As Table 2 for a 2-shells configuration (5cm LaBr3 + 15cm CsI).

2.3 Inner versus outer shell performances

In order to investigate the pertinence of a two-shell configuration, aside from the total energy collected in the whole detector bulk E_{det}, the partition of the energy deposited in the two shells separately has to be carefully studied. In order to match the PARIS collaboration requests, *the inner shell should constitute a powerful multiplicity filter and provide the energy sum* with good resolution. Thus, it should be particularly efficient for low-energy γ-rays (up to about 2MeV). *The outer shell is dedicated to the detection of high-energy photons* (mostly from the GDR decay) *and the required resolution is less severe*. The *'transparency' of the inner shell* as function of the incident γ-ray energy and its influence for energy collection in the outer shell will be investigated in detail. All together will condition the accuracy of the reconstruction algorithm and, consequently, the final energy resolution. We note that the availability of *a second shell might provide some useful information for tracking* particles. Indeed, it gives, in some sense, insight into the depth of the interaction and might be used in connection with the angle information for recovering the true initial energy E_{inc}. That might be of particular benefit for the accuracy of the reconstruction procedure. For some specific physics cases (e.g. radiative capture reactions) the energy resolution has to be good enough for high energy γ-rays as well. That requires that *a finite percentage of incident high-energy photons should already stop in the inner shell*. It implies a still reasonable efficiency of the inner shell at high energy.

For those incident γ-rays which deposit their whole energy in the ensemble of the two layers, Fig. 7 shows the probability for full absorption in one of the two shells separately for several two-shell configurations made of LaBr3 and CsI. Fig.8 presents similar spectra for the combination LaBr3+BGO. The total efficiency and the one of the outer shell are, of course, larger in Fig.8 as compared to Fig.7. Yet, and as stated earlier, although efficient for

multiplicity measurements, BGO is excluded for PARIS. Furthermore, CsI seems by far worse. Materials such as NaI and BaF2, which have densities comparable to CsI, shall not be disregarded neither as far as efficiency, energy deposit and angular patterns are concerned. According to simple density considerations, replacing the 15cm thick CsI outer shell considered in most part of the present with a 17cm thick BaF2 layer (as it is the case in HECTOR) would lead to slightly larger overall efficiencies and more 'compact' particle showers. For deciding on the outer shell material, additional considerations (time resolution, possibility of pulse shape analysis, light yield, wave length depending on the APD or PM's electronics, cost, etc) have to be taken into account.

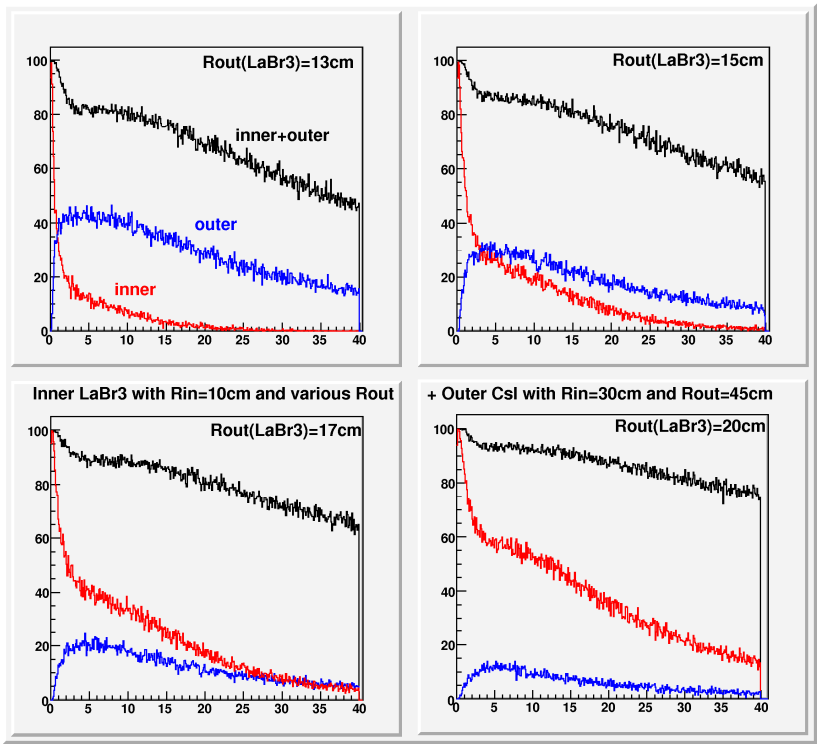

Fig. 7: Probability for full absorption as a function of E_{inc} for a LaBr3 layer with R_{in}=10cm and R_{out}=13cm (left), 15cm (middle), 20cm (right) followed by a CsI layer with R_{in}=30cm and R_{out}=45cm. Black curves refer to full absorption in the ensemble of the 2 shells (identical to Fig.3) while the red and blue curves correspond to full absorption in either the inner or outer shell, respectively.

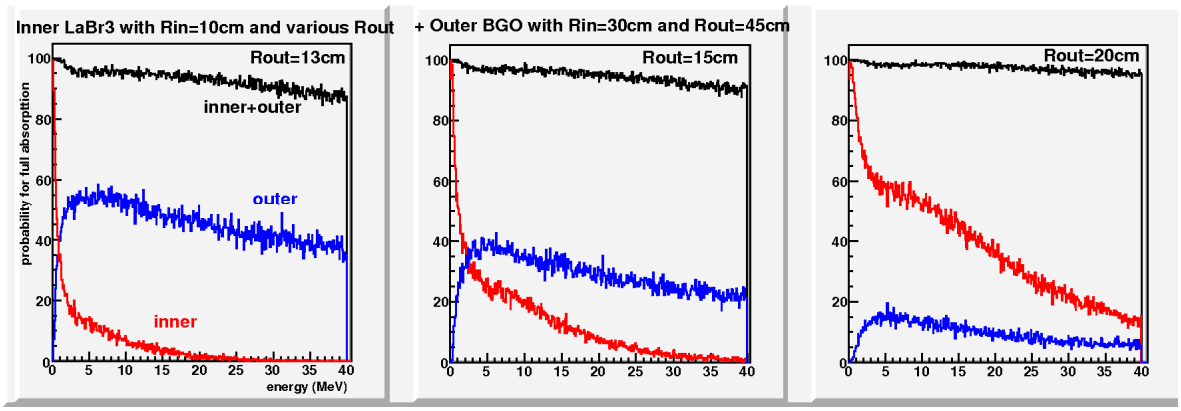

Fig. 8: Identical to Fig.7 replacing the material of the outer shell with BGO for R_{in}(LaBr3)=3, 5 and 10 cm.

Let us focus on the results obtained for LaBr3 coupled to CsI presented in Fig.7. For a 3cm thick inner LaBr3 layer, about 40% of the gamma rays with energies up to 2MeV are *fully* absorbed in the inner shell. Above 10MeV, less than 40% of the events deposit their *whole* energy in the outer shell, while less than about 5% of the events do not escape the inner shell, i.e. are still fully absorbed in the inner shell. For a 5cm thick inner LaBr3 layer, nearly 50% of the gamma rays with an energy of 2MeV are fully absorbed in the inner shell. Between 10 and 25MeV, still 5 to 15% of the events deposit their whole energy in the inner shell, while for about 20% of them all the energy is deposited in the outer shell. For a 10cm thick inner LaBr3 layer, up to 15MeV, 45% or more of the γ rays are fully absorbed in the inner shell. The probability for full absorption in the outer shell remains well below 10% at high energy. In this case, at first glance, the utility of the outer shell might be questioned at all. However, although negligible for full absorption events, its contribution for restoring the true initial energy by add-backing the deposit in the two layers is probably crucial for 'getting back' a non-negligible part of events. Note that the above numbers correspond to full absorption as defined by $E_{det} > 99\% E_{inc}$. Slacking slightly out this severe criterion (for instance, accounting for the limited energy resolution) changes the previous numerical values, but the main conclusions remain valid (see below).

Increasing the radius of the inner LaBr3 shell, of course, favours full absorption in the inner shell with respect to the outer layer. The influence of the first LaBr3 shell appears to be of crucial importance. According to Fig.7, a **compromise has to be made for large full absorption probability of low-energy γ-rays in the inner shell** (multiplicity and energy sum job)**, while maximizing transparency for the high-energy photons, *but*, at the same time, keeping a finite reasonable probability for full absorption at high energy in the inner shell** for those physics cases where the resolution at high energy is mandatory.

Increasing the thickness of the outer shell obviously permits increasing the overall efficiency of the device. In Fig.9, a 20cm thick CsI outer layer is observed as nearly equivalent (at least, in terms of energy deposit) to a 15cm thick outer BGO shell. It shall be noticed that the magnitude of the gain obtained when increasing the thickness of the outer CsI shell strongly depends on the thickness of the inner LaBr3 layer. When the latter exceeds about 5cm, the gain might not be so worthwhile, since either a sizeable part of the events is already absorbed in the inner shell, or the percentage of events sharing their energy deposit between the 2 shells considerably increases. Conversely, below about 5cm for the inner shell thickness, one still gains a lot in the overall efficiency and, more importantly, in the probability of full absorption in the outer shell at high energy (about a factor of 1.5-2 at $E_{inc} \sim 35$MeV). At the same time, a finite (reasonably large?) amount of high-energy γ-rays remains fully absorbed in the inner shell as required for achieving a good resolution at high energy in some PARIS physics cases (above 10% for the $E_{det}>99\% E_{inc}$ absorption criterion, i.e. even more for the more realistic $E_{det}>95\% E_{inc}$ absorption condition, see below).

The difference between the sum of the black curve and the blue and red curves corresponds to events which energy deposit is shared between the 2 shells. A compromise has to be found for optimising the energy partition between the shells, minimizing tricky energy sharing. Furthermore, the study of the spread in angle of the shower generated by a primary γ-ray will define the most suited segmentation (see sections 2.5 and 2.6). All this will be investigated in connection with the determination of the reconstruction algorithm. As already mentioned,

along this task, a two-shell configuration seems useful, providing a rough segmentation in depth.

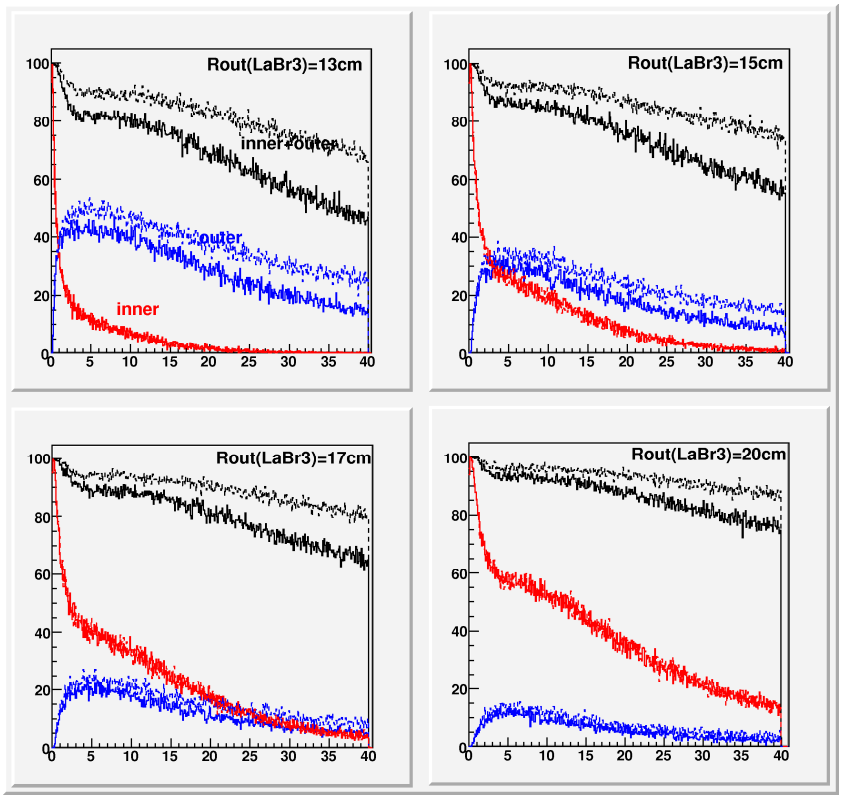

Fig. 9: Identical to Fig.7 (full lines) with, in addition, the results for an outer CsI shell with R_{in}=30cm and R_{out}=50cm (dashed lines).

So far, full absorption was fulfilled provided that more than 99% of E_{inc} is deposited in the detector. As briefly touched above, according to the limited energy resolution (minimum of 2-3%), such a strong condition might not be realistic. We shall thus check to what extent the above conclusions do depend on the precise definition assumed for full absorption. Fig. 10 presents the same quantities as in Fig.7-9 with less severe definitions of full absorption: The level of tolerance is set to 95% of E_{inc} (dashed lines) and 90% (full lines). Comparing Fig.7 and Fig.10, we conclude that the above conclusions are expected to *qualitatively* hold for alternative reasonable definitions of full absorption. This result is not so surprising according to the numbers of Table 2. Note in Fig.10 a kind of 'kick' between 0-5MeV: that is an artefact related to the full absorption gate for events with escape of an annihilation photon. Indeed, as observed in the left panel of Fig.11, the precise location of the kick depends on the incident energy (NB: 511 keV represents around 5% of 12 MeV, 10% of 5 MeV, 20% of 2.5 MeV, 30% of 1.7 MeV, what implies a kick around 5(12) MeV for the condition $E_{det} > 90(95)\%$ of E_{inc}). Since 511 keV represents about 1% of ~50 MeV, it did not appear in our previous figures where the full absorption condition was set at 99% of E_{inc}. The origin of this artefact becomes even more obvious when considering discrete γ-rays below and above the threshold energy for pair creation (not shown).

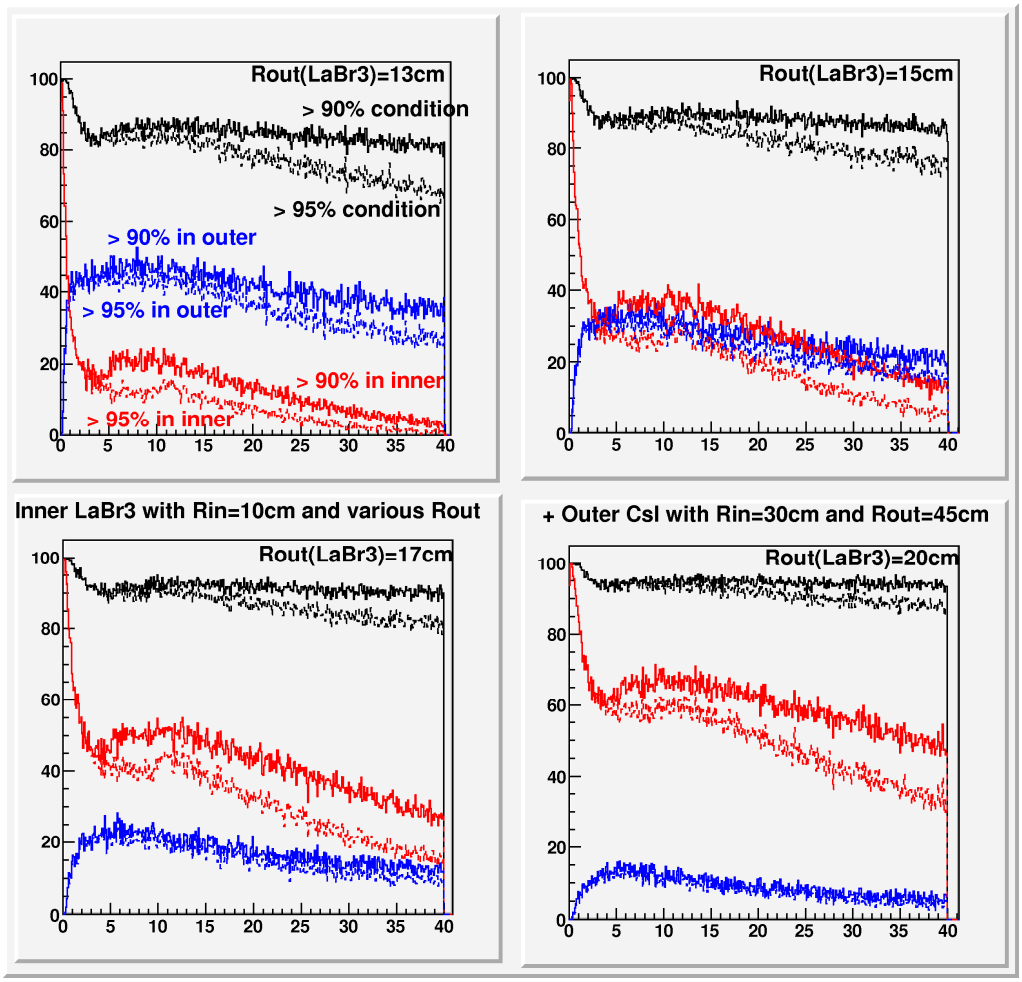

Fig. 10: Identical to Fig.7 replacing the definition of full absorption by E_{det} > 90% of E_{inc} (full lines) or E_{det} > 95% of E_{inc} (dashed lines).

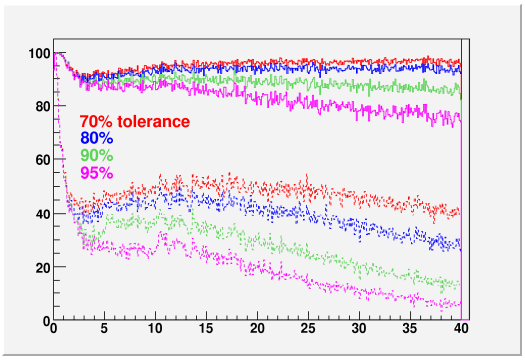

Fig. 11: Full absorption probability in the (inner+outer) device (full lines) and in the inner shell alone (dashed liens) for various definitions of full absorption.

2.4 Energy sharing

To deepen further the influence of the inner shell, let us consider in more details how the energy deposit is shared between the two layers as a function of the incident photon energy E_{inc}. *We presently restrict to those events which are fully absorbed in the ensemble of the two*

shells, with the absorption condition set at 95% of E_{inc}. According to Table 3, the restriction to the sub-set of events depositing at least 95% of E_{inc} should be representative of the complete data set. Still, the influence of the precise absorption criterion will be studied further below. In the right column of Fig.12, for various incident photon energies E_{inc}, we display the correlation between the energy in MeV deposited in the inner (E_{inner}) and outer (E_{outer}) shell. The left column of the figure presents the percentage of energy deposited in each shell, separately. I.e. the red (blue) histograms correspond to the distribution in % of the quantity E_{inner}/E_{inc} (E_{outer}/E_{inc}). The restriction to events which are fully absorbed in the detector bulk implies that peaks located at 100% refer to events which deposit their whole energy *exclusively* in one of the two shells (respectively, in the inner and outer layer for the red and blue peaks at 100%). In the same line, a peak at (E_{inc}-511)keV in a given shell is associated to a peak at 511keV in the other shell *provided* that the 511keV diffused photon is fully absorbed in the counterpart layer (neglecting multi-diffusion). Hence, for E_{inc}=5MeV, the red peak at E_{inner}/E_{inc}=89.8% is in most cases correlated to the blue peak at E_{outer}/E_{inc}=10.22% (NB: 511keV corresponds to 10.22% of 5MeV). In general, the intensity at $(E_{inner}-\varepsilon)/E_{inc}$ in the red histogram is similar to the one at ε/E_{inc} in the blue spectrum. The restriction to fully absorbed events delimits a straight line along the diagonal for the (E_{outer}, E_{inner}) correlation spectra.

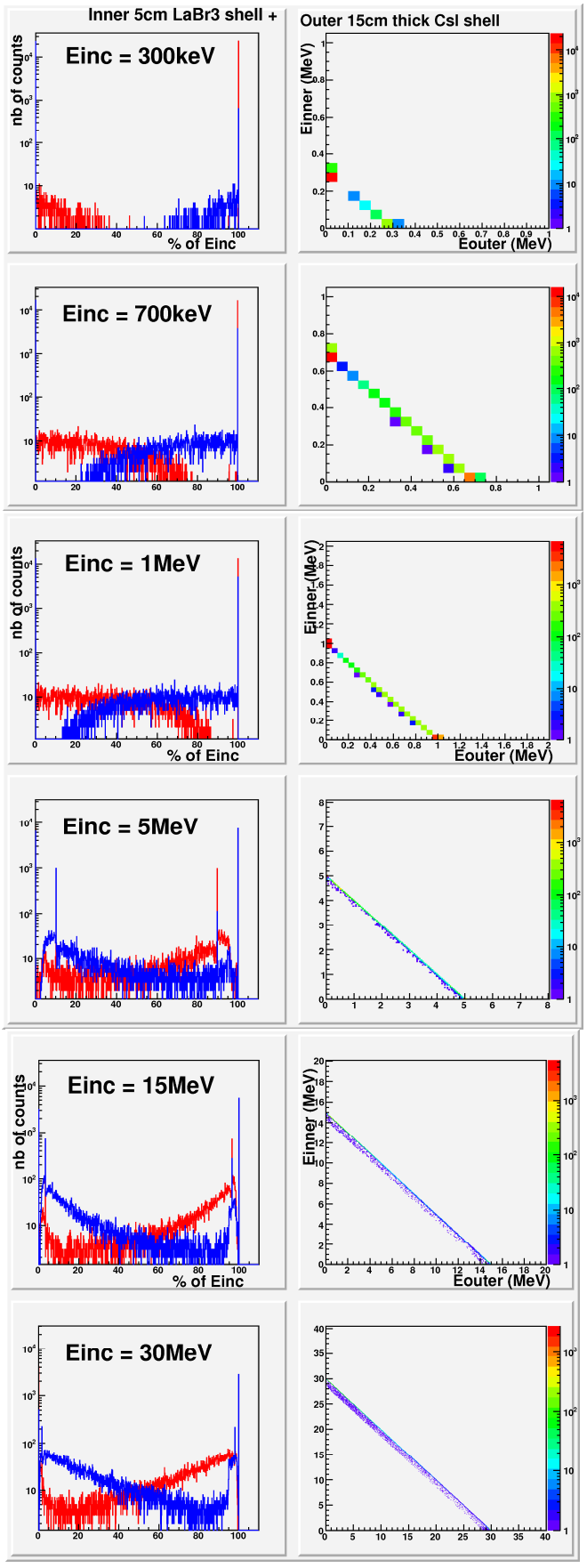
Inner 5cm LaBr3 shell +
Outer 15cm thick CsI shell
Einc = 300keV
Einc = 700keV
Einc = 1MeV
Einc = 5MeV
Einc = 15MeV
Einc = 30MeV
nb of counts
% of Einc
Einner (MeV)
Eouter (MeV)

Fig. 12: Left column: Percentage of energy deposited in the inner (red lines) and outer (blue lines) shell for several E_{inc} as indicated, for a two-shell configuration (5cm of a LaBr3+ 10cm of CsI). Note the identical scale for the histograms in the left column: The decrease of the number of counts with increasing E_{inc} is, of course, caused by the decrease of full absorption. Right: Correlations between the energy (in MeV) deposited in the inner vs. the outer shell for the indicated E_{inc}. The full absorption criterion is set at $E_{det} > 95\%$ of E_{inc}.

For γ-ray energies below about 1-2MeV, energy sharing between the 2 shells is very rare. In the photoelectric regime, the γ deposits its whole energy in either the inner or the outer shell. In the Compton domain, particles start diffusing from one shell to the other. A precise survey of the probability of this phenomenon is in progress (see also section 2.8). As noted above, at higher energies, in the pair creation domain, peaks related to the escape of the annihilation photon(s) in one of the shells followed by its potential detection in the other shell start to emerge. From Fig.12, it may be speculated that, **below 5MeV, actual energy sharing between the 2 shells remains weak, if not negligible at all. Energy sharing is mainly caused by the diffusion of the annihilation photon(s). Such events are readily recognizable, what may facilitate their reconstruction**. **At higher energies, the deposit pattern is less dominated by diffusion of annihilation photons, and better partitioned between the 2 shells, although the probability for comparable energy collection in the 2 layers seems to remain rather low**, **the sharing being preferentially asymmetric.**

Similar percentage of energy deposit distributions are displayed for an outer CsI thickness of 20cm (instead of 15cm) in Fig.13, and for an outer layer made of NaI (instead of CsI) in Fig.14. The above conclusions qualitatively hold for these configurations as well. The difference between the partition pattern when taking either NaI or CsI for the outer shell is nearly negligible. That corroborates the **dominant importance of the inner shell**, at least when made of LaBr3. Efficiency arguments based on Fig.2 suggest that BaF2 for the outer shell would lead to similar spectra. As already mentioned, depending on additional considerations for NaI, CsI or BaF2, the pertinence of one or another material shall be judged.

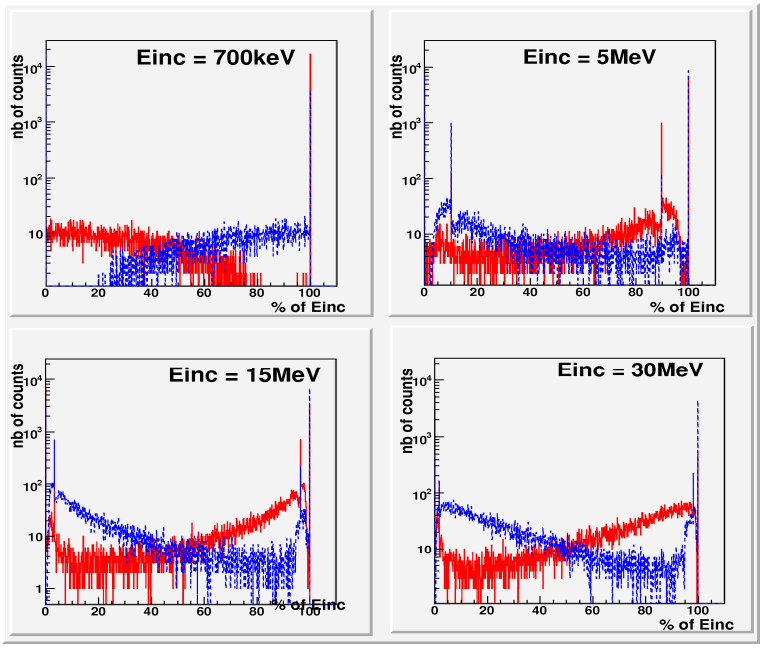

Fig. 13: Similar to the left column of Fig.12 for an outer shell of CsI layer with R_{in}=30cm and R_{out}=50cm.

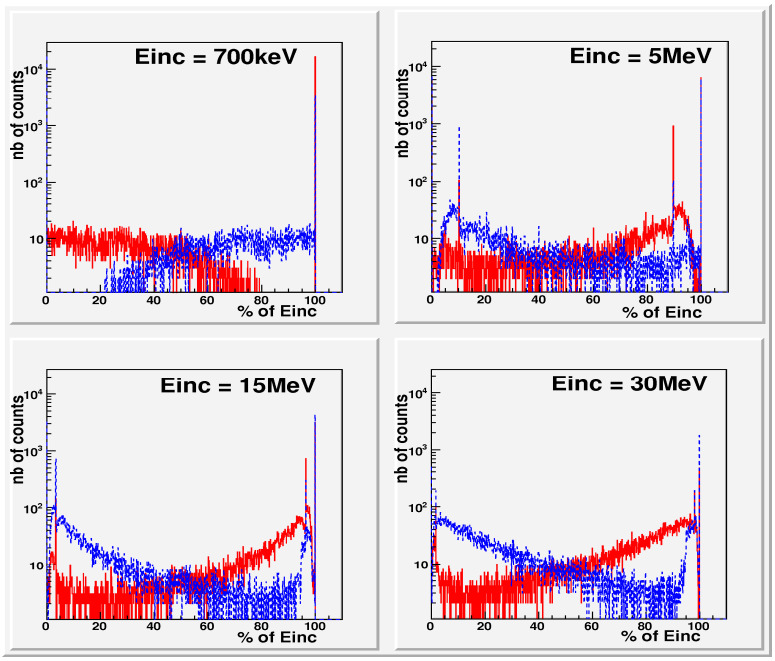

Fig. 14: Similar to the left column of Fig.12 for an outer shell of NaI layer with R_{in}=30cm and R_{out}=45cm.

In Fig.15 and 16, the energy deposit patterns are finally shown for full absorption criteria set, respectively, at 80% and 60% of the true initial energy E_{inc}. The broader diagonal bands in the (E_{outer}, E_{inner}) correlations are, of course, related to the less strong absorption criterion. The fact that, with these criteria, the energy partition between the 2 shells seems to be more equilibrated at high energy is rather an artefact caused by the definition used for absorption than of physical origin. Anyhow, nearly similar energy deposits in the 2 shells are minority.

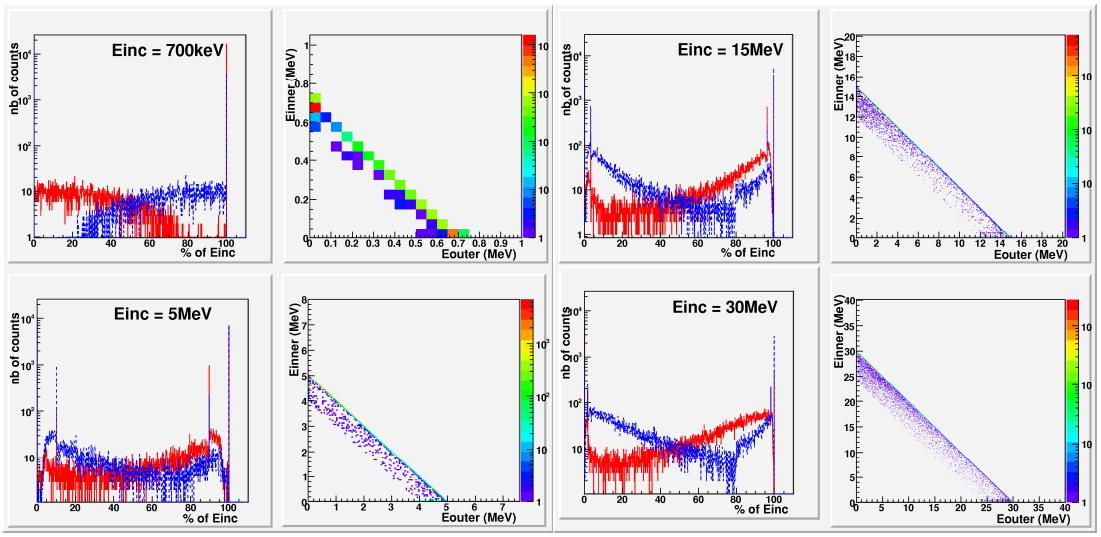

Fig. 15: Similar to Fig.12 when full absorption if defined as E_{det} > 80% of E_{inc}.

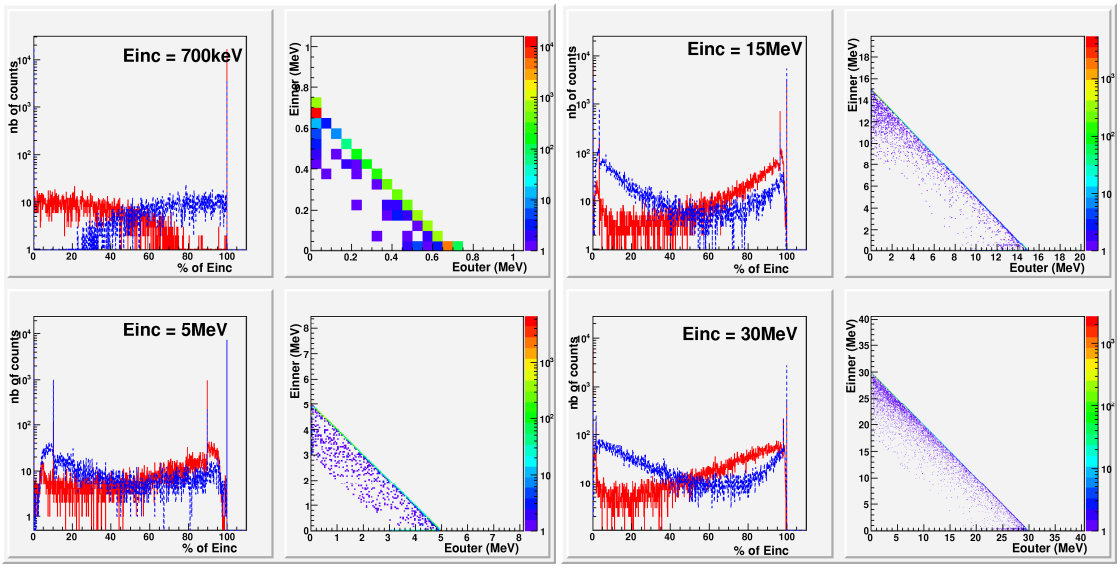

Fig. 16: Similar to Fig.12 when full absorption if defined as $E_{det} > 60\%$ of E_{inc}.

The natural next step is to see how the above observations can be deepened when introducing segmentation and correlating the energy and angular information.

2.5 Angular spread

The scattering in the energy deposit pattern has to be investigated in close connection with the angular spread of the shower generated by the incident photon. Aside from its relevance for Doppler correction, the latter is also of great help for reconstructing the true initial energy. It is, of course, crucial as well for defining the suited segmentation. In Fig. 17 the angular (ϑ, ϕ) spread of the shower created by the incident photon (and including all secondary particles) is shown for typical incident energies and two geometries. The ϑ and ϕ angles are defined with respect to the direction (ϑ_0, ϕ_0) of the primary photon. In Fig. 18, the angular correlations are shown *weighted* this time by the energy deposit *with respect to the incident energy* E_{inc}. We shall notify that in Fig.17 and 18, no selection is made on the amount of energy absorbed in the bulk of the detector. Alternative energy weighting, namely *with respect to the energy indeed deposited in the detector* bulk, will be considered later on (see namely section 2.8). Yet, since the 20cm thick detectors assumed in Fig.17 and 18 are rather efficient (cf. Fig.2 and 3), and as has been checked, the general trend is presently not strongly altered by the precise definition of the weighting.

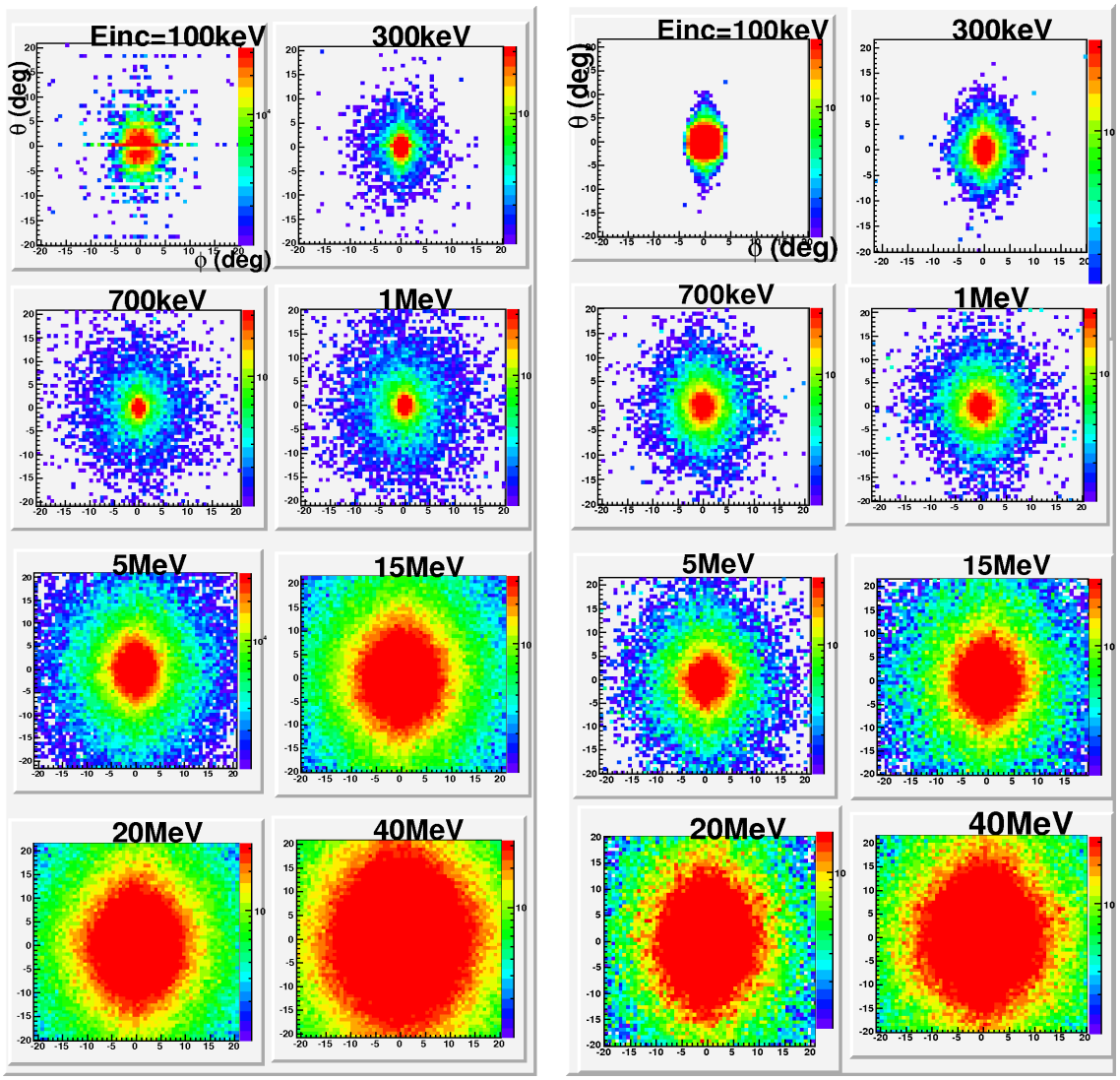

Fig. 17: Angular (ϑ, φ) spread in ° for various E_{inc} as indicated. In the left panel, a single 20cm-radius full sphere of LaBr3 is considered. In the right panel, a two-shell device made of an inner LaBr3 layer with R_{in}=10cm and R_{out}=15cm followed by an outer CsI layer with R_{in}=30cm and R_{out}=45cm is assumed. No selection is applied on the % of E_{inc} deposited in the detector. Note the logarithmic z-scale.

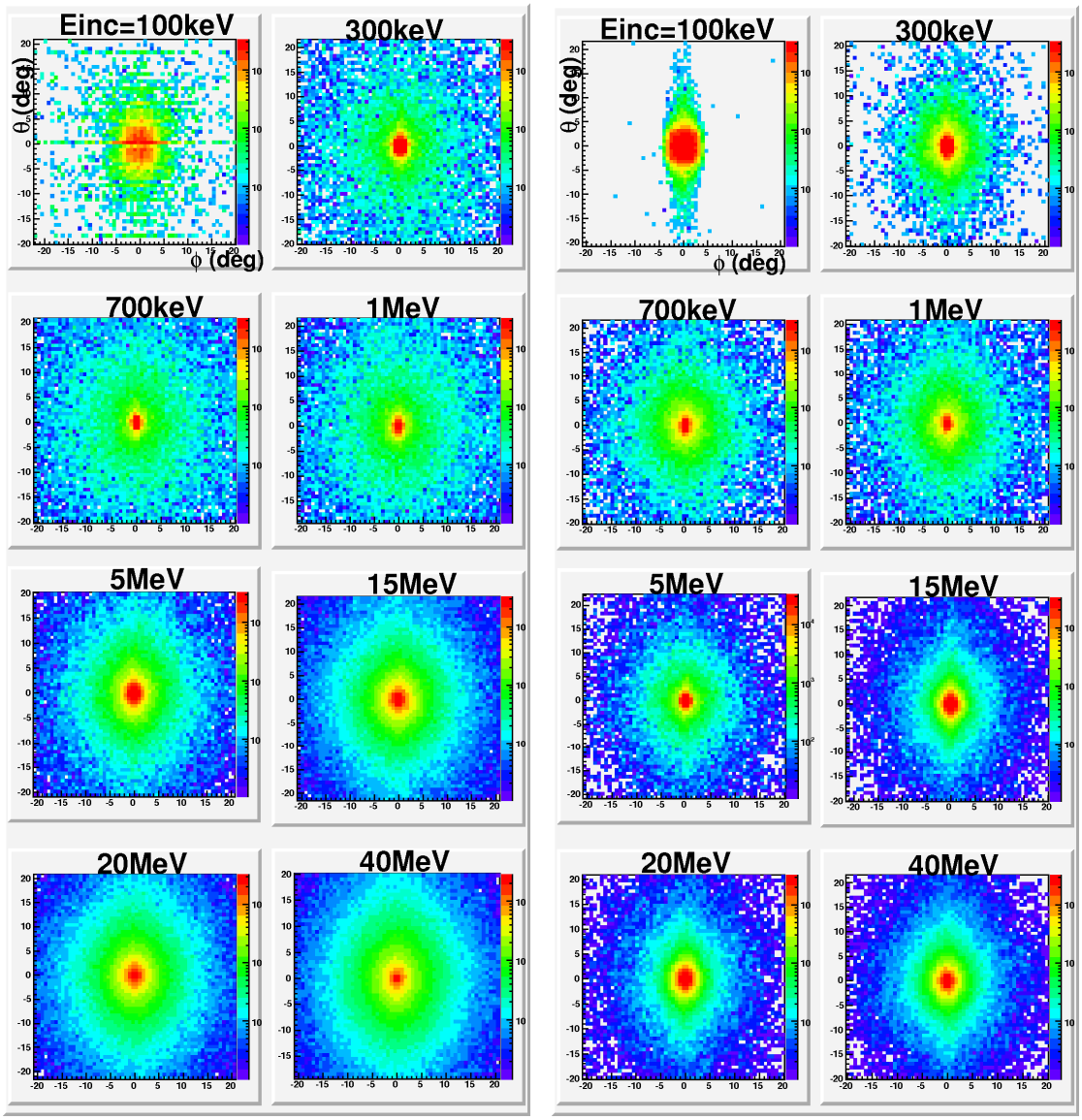

Fig. 18: Identical to Fig.17 weighting each interaction point by the percentage of energy deposited at the point with respect to the full incident energy E_{inc}.

When considering a full spherical geometry (left panels of Fig.17 and 18), the angular spread is, of course, larger than for $R_{in}\neq 0$ (right panels of Fig.17 and 18). As expected, if *not* weighted by the energy deposit (see Fig.17), the angular distribution of the interaction points increases with increasing energy: The larger the incident energy is, the more numerous secondary particles are, the larger the dispersion might be. When weighting each interaction point in the detector by the percentage of energy deposited relative to E_{inc} (see Fig.18), the trend in the angular pattern as a function of E_{inc} changes. In particular, the shower strongly shrinks. The FWHM of the spread in ϑ and ϕ does not exceeds about 5-6° for the two-shell configuration. Hence, although some energy might be deposited quite far away from the incident photon direction, there is a **large probability that most of the energy is deposited in a limited angular cone around the initial direction**. As the crystal is not segmented in the present simple simulation scheme, it is not possible to determine which crystal element a given amount of energy deposit belongs to. In addition, a more precise quantification of the

percentage of energy deposited as a function of angle has still to be done. Yet, according to customary crystal sizes, the present observation is encouraging, reminding that a 1 inch per 1 inch crystal subtends an angle of about 14° at 10cm.

The evolution of the angular pattern as a function of incident photon energy may be compared with the scattering expected for the various interaction processes involved. Some interaction processes deposit part (Compton scattering) or all (photoelectric effect) of the incident energy close to the first interaction point (provided the range of secondary electrons remains small, what is rather realistic at not too high energy). For Compton interactions, the emerging γ-ray changes its direction and can deposit energy rather far away from the first interaction track. In case of pair creation, energy may be deposited far away from the incident γ-ray path as well. Nevertheless, as compared to what happens along the Compton process, the ionisation of the medium by the progressive energy loss of the electron/positron pair is quite well focused (except for the final annihilation of the positron leading to photons emitted back to back). In addition, pair creation can occur, not only at rest, but also in flight, what even more focuses the resulting shower. As a consequence, the spread of the energy-weighted shower in the Compton interaction energy domain[1] is expected to be larger than at higher energy where pair creation prevails. The angular dispersion of the shower is observed to saturate at the highest incident energies, corroborating the focusing of the shower generated by pair creation. The presumable wider spread in the intermediate Compton regime is not as obvious (see also discussion below). According to all these considerations, the largest angular spread observed for the photoelectric low-energy regime (E_{inc}=100keV in Fig.18) can be surprising. To understand this observation, the limited information carried away in (ϑ, ϕ)-like correlations should be emphasized. In particular, it is stressed that such spectra do not contain information on the *interaction depth*. Hence, the photoelectric effect which, for an incident low-energy γ-ray, occurs very close to the surface of the detector can be characterized by a sizeable angle due to pure geometrical considerations (the nearer the point, the larger the subtended angle). Conversely, the actual larger spread inherent to Compton scattering can appear smaller because the interaction occurs deeper into the detector bulk. Thus, additional quantities are mandatory in order to get a more *complete picture of the topology of the events*. Some of such are proposed in the following sub-sections.

2.6. Interaction depth

Investigating the interaction depth is obviously primordial for defining the suited length of the crystals ensuring a reasonable probability of full absorption. It is also important in connection with the angular shower spectra for characterizing the precise pattern of the energy deposit as a function of incident energy and reconstruct properly each event. The interaction radius depth is defined here as $\sqrt{(x^2+y^2+z^2)}$: it characterizes the extent of the shower in the detector bulk in depth but does *not* contain memory on the initial direction. In Fig.19 the distribution of this radius for all interaction points generated by a primary photon, weighted – or not - by the energy deposit is shown for a few E_{inc} values. Including the information on the amount of energy deposited at each interaction point is seen to be critical. In Fig.20, for the energy-weighted distributions of Fig.19 - left panel, a zoom on the inner shell region and on the beginning of the outer shell sheds light on the evolution of the interaction pattern with increasing energy. As expected, low-energy photons interact near the surface of the inner

[1] For CsI, NaI and Ge, Compton scattering is dominant in the energy [700keV, 7MeV], [200keV, 2MeV] and [200keV, 5MeV] domains, respectively).

detector, while a progressive depletion of this region is observed when E_{inc} rises. Of particular interest is the energy deposit pattern in the inner vs. the outer shell as a function of incident energy. Up to about 5 MeV, the photon loses most of its energy in the inner shell, and only a remaining part at the beginning of the outer layer. At higher energy, this scheme changes. In particular, as it is for the inner shell, a progressive depletion of the zone near the surface of the outer layer is observed with increasing E_{inc}. One may speculate that this corresponds to events for which the inner shell is completely transparent. Yet, there could also be a contribution from secondary high-energy γ's generated along the shower from high-energy electrons and positrons. According to the mean free path of the photon at high energy (cf. discussion of section 2.2 and Appendix A) such a contribution is likely to explain Fig. 20. Further investigations, namely concerning the correlation between the energy loss and the *sequence of fired shells*, are in progress to settle this point.

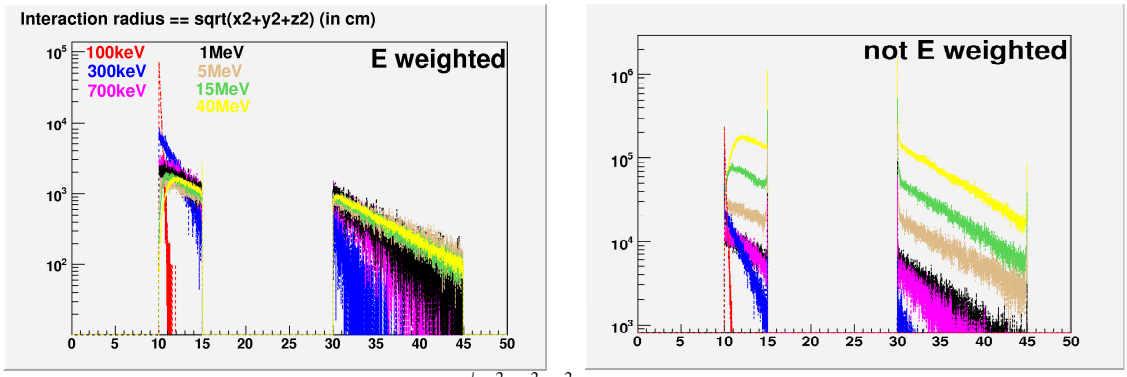

Fig. 19: Left panel: Interaction radius depth $\sqrt{(x^2+y^2+z^2)}$ in cm for each interaction point into the detector bulk delimited by an inner LaBr3 layer with R_{in}=10cm and R_{out}=15cm and an outer CsI layer with R_{in}=30cm and R_{out}=45cm. Various E_{inc} are considered. No selection is applied on the % of E_{inc} deposited in the detector. The interaction point is weighted by the energy deposit. Right panel: Identical to the left panel but without weighting the interaction point by the percentage of energy deposited.

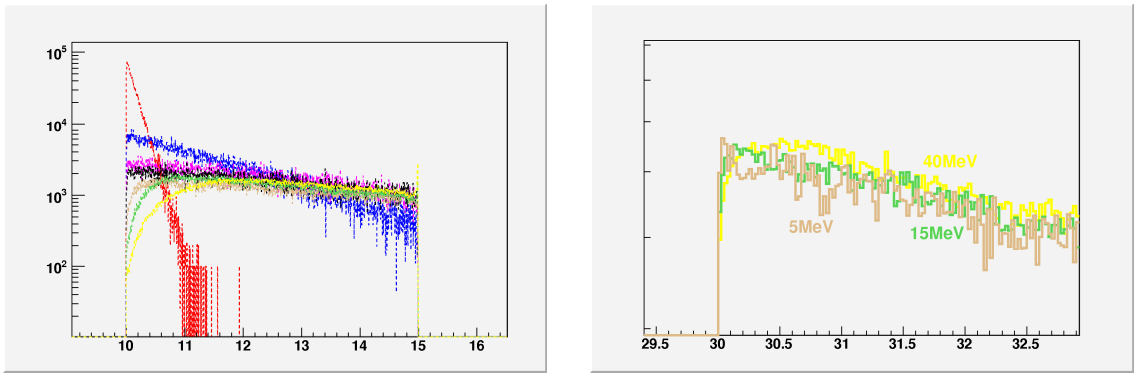

Fig. 20: Zoom of the left panel of Fig.19 on the inner layer (left) and the beginning of outer shell (right).

2.7. Radial dispersion

To characterize the pattern of the energy deposit, the dispersion of the shower is investigated in more detail in Fig.21. There, the distribution of the so-called *radial dispersion* is plotted for a few incident energies and two geometries. Radial dispersion is defined presently *for each interaction point* as the distance of the interaction point with respect to the incident direction

($\approx \sqrt{(x^2+y^2)}$ with respect to the incident track shoot along the z-direction). The mean value of the radial dispersion differs more and more sizeably from zero with increasing energy. The zooms displayed in Fig.22 seem to corroborate the fact mentioned in section 2.5 about the relative dispersion associated to the various processes involved. First, there is a strong saturation of the dispersion at high energy. Second, it is not obvious that the dispersion is largest in the Compton scattering energy range (cf. discussion in section 2.4). The fact that the difference between the dispersion in the Compton vs. pair creation regime is smaller than suggested above may partly be explained by [i)] the maximum of the Compton cross section peaked at small angles (retro-diffusion being minority) and [ii)] the increasing focusing of the Compton shower with increasing energy. Including the increase of the number of secondary particles and the unknown accurate dependence on the material, all together leads to a tricky interplay.

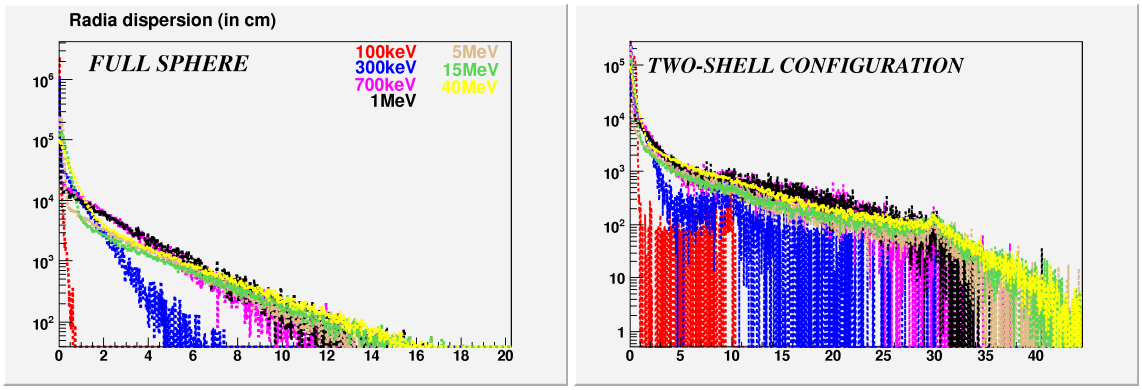

Fig. 21: Radial dispersion (in cm) of all interaction points of the shower generated by typical incident photons which energies are indicated. A full single LaBr3 sphere of 20cm radius is considered in the left panel, while an inner LaBr3 layer with R_{in}=10cm and R_{out}=15cm followed by an outer CsI layer with R_{in}=30cm and R_{out}=45cm is considered in the right panel. Each interaction point has been weighted by the associated energy deposit.

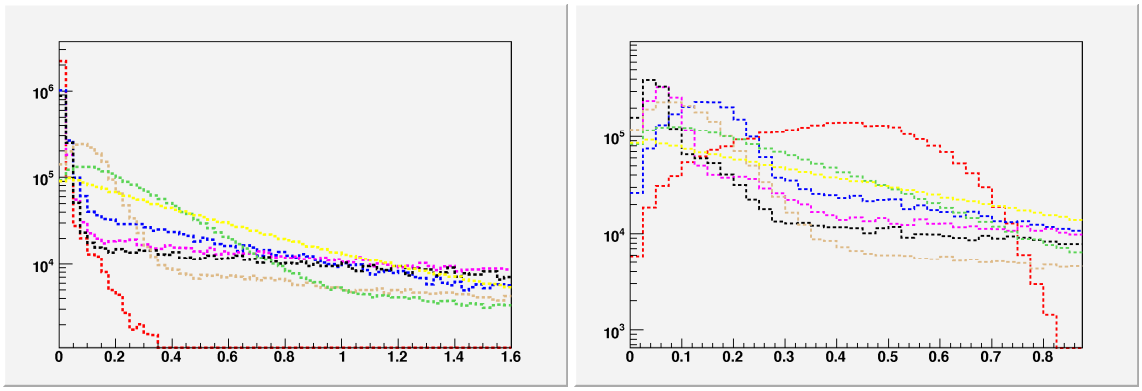

Fig. 22: Identical to the to Fig.21 with a zoom in the small dispersion range.

2.8. Average expansion of the energy deposit pattern

In contrast to the above quantities constructed with *all* interaction points of the shower generated by an incident photon, a more general view point is given in Figure 23. There, the *average* interaction vector *R per* primary particle is projected along the longitudinal $R_{//}$ and transverse $R_{\perp}$ incident direction. It is defined as the average over all interaction point vectors

related to a given primary particle and weighted by the percentage of energy deposit with respect to the total amount of energy detected E_{det} (cf. discussion in section 2.5) i.e.

$$\overrightarrow{R} = \frac{\sum_i \overrightarrow{r}_i \cdot e_i}{\sum_i e_i}$$

While the vector r_i associated to *all* the interaction points i generated by the primary photon has been considered in the observables of section 2.5-2.7, presently we construct the *mean* vector given by the ensemble of interaction points per incident particle. In case of a two-shell geometry, values for R falling in between the two layers are thus possible.

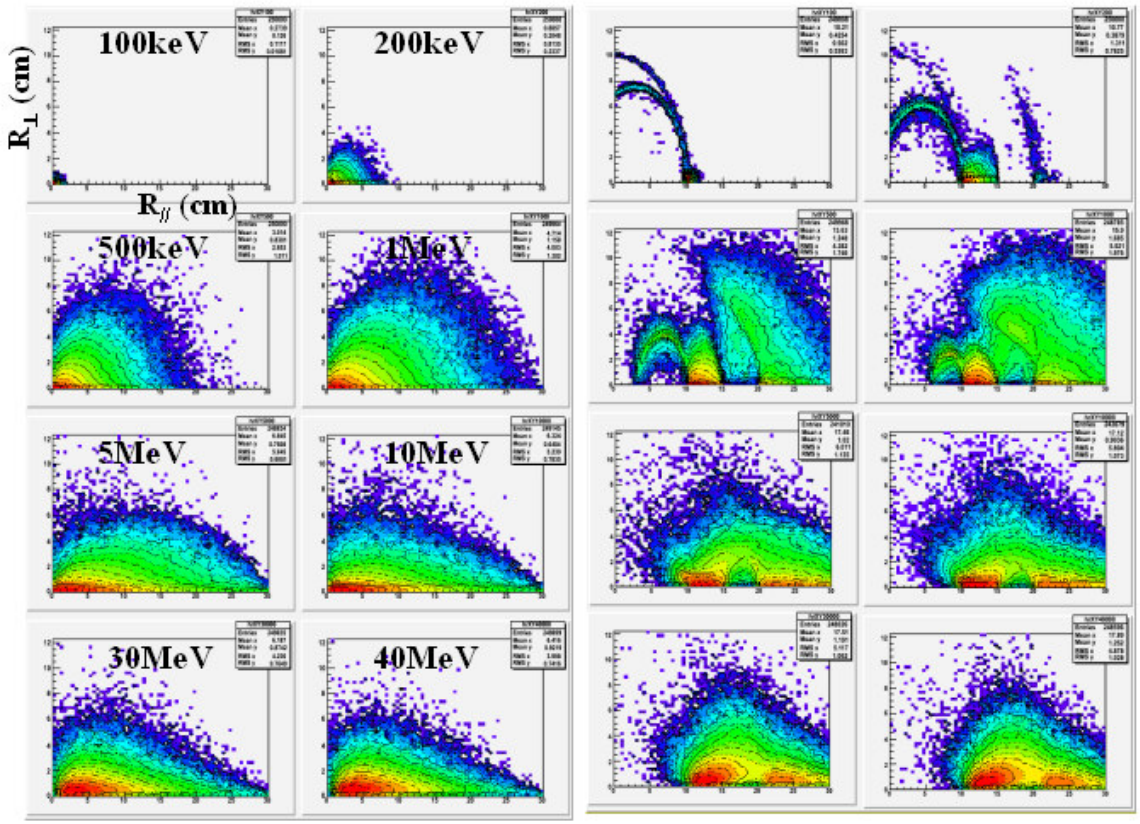

Fig. 23: Left panel: Correlation between the longitudinal $R_{//}$ and transverse $R_{\perp}$ average interaction vector weighted by the energy deposit (see the text) for the indicated incident energies and a full single LaBr3 sphere of 30cm radius. Right panel: Identical to the left panel for a two-shell geometry with an inner LaBr3 layer with R_{in}=10cm and R_{out}=15cm followed by an outer CsI layer with R_{in}=20cm and R_{out}=30cm. Note the logarithmic z-scale.

Let us start with a single full sphere geometry (left panel of Fig.23). As suggested in the previous sections, the general scheme is as follows. In the photoelectric energy domain, the range of the incident photon inside the detector bulk is short ($R_{//}$>2cm) and deviation from the initial track is negligible ($R_{\perp}$<1cm). As soon as Compton interactions set in, multiple scattering leads to a fast increase of both $R_{//}$ and $R_{\perp}$. At higher energies, pair creation dominate, what shows up in a sizeable decrease of the radial expansion of the shower, which finally saturates. These conclusions remain valid in the case of two concentric shells. Yet, the

latter geometry considered in the spectra of the right panel of Fig.3 deserves some more attention. In the photoelectric domain, in addition to the quickly absorbed photons, there appear lines caused by some Compton retro-diffused photons. With increasing energy, as for the single shell geometry, multiple Compton scattering increases $R_{//}$ and $R_{\perp}$ *in each individual shell*. At the same time, the *diffusion between the two shells* gets wider and increases in intensity. Finally, in the pair creation regime, there is again a stronger forward-focusing Retro-diffusion disappears for the inner shell. For the outer shell, the situation is more complex. To pin down the topology of the events, further studies dedicated to determine the sequence of interaction of the diffused particles are in progress: How is the energy shared when the initial pair creation takes place in the inner shell or in the outer layer?

3. Conclusions

The primary simulations performed for the PARIS calorimeter with the GEANT4 package and their analysis in the ROOT framework have been presented. The package provides the useful starting tools for investigating the geometrical design and suited segmentation of the device according to the various physics cases foreseen to be studied at PARIS.
So far, a survey of global quantities has been studied. For a two-shell configuration, interesting observations have been made, namely about the **crucial influence of the inner shell**. The idea of **two concentric layers seems to be rather pertinent**, as suggested by the results obtained with an inner LaBr3 layer followed by an outer CsI shell:

- The percentage of fully absorbed events in one of the 2 shells has been found rather large.
- A two-shell design is relevant provided the inner shell is not too much absorbent. In this way, the inner shell fulfils its calorimeter job, while the outer layer is devoted to the detection of high-energy photons.
- Aside from events which are fully absorbed in either of the two shells, a sizeable percentage of fully absorbed γ-rays in the whole detector bulk share their energy deposit between the 2 layers. Provided we are able to properly reconstruct the energy partition, the global performances of the array can even be further enhanced.

The present results suggest as a compromise an upper limit for the thickness of the layers. Fine investigations are nonetheless still required to determine the optimal size of the first and second shells as well as the most suited material.

In addition to the crude information on the interaction depth given by the shells, the array is segmented in (ϑ, ϕ). The topology of the events in such a "3 dimensional space" is crucial to optimise the reconstruction algorithm to be used. Energy deposit patterns, studied as function of the incident energy, gave insight into:

- how precisely the incident energy is shared between the 2 layers; namely, a rather asymmetric energy partition seems to prevail up to high incident energy;
- how the annihilation photon(s) diffuse from one shell to the other. According to our first studies, a sizeable proportion of the 511 keV photons escaping from a given layer are finally detected in the counterpart shell;
- what are the precise geometrical shape (depth, angle) of the shower generated by the incident photon. Along this point, Compton scattering events might deserve much attention.

4. Perspectives

Aside from the required simulations tackled in the above text and which are either already under study or will be investigated in priority, additional important studies are in progress:

- to estimate the gain in performance of the device (probability of full absorption) when taking into account diffusion from annihilation photon(s) between the 2 shells;
- to determine the precise topology of events for which either the inner or the outer shell is fired first (i.e. profit from the sequence of fired layers to reconstruct events);
- to define precisely the optimal thickness of a potential inner LaBr3 shell;
- to investigate the most suited (ϑ, ϕ) segmentation allowing a proper reconstruction of the multiplicity;
- to study different combinations of materials and/or geometries. In particular, the **concept of a nearly complete inner shell of LaBr3 combined with an outer shell consisting, alternatively in angle, of a thin LaBr3 layer and a thick e.g. CsI layer shall be deepened**. The inner shell would constitute an efficient calorimeter together with an outer shell which would efficiently stop high-energy photons over part of the solid angle and with a reasonable energy resolution. For about half of the solid angle, the outer thin LaBr3 shell would permit increasing the probability of absorbing high-energy γ-rays and achieve at the same time the good resolution at high energy as required for some physics cases of PARIS;

Appendix A

In order to get an idea about the interaction of a photon with LaBr3 material as function of the γ-ray energy, the cross section and mean free path associated to the various processes involved are given in Tables A.1 and A.2 for La and Br, respectively.

Material: Lanthanum density: 6.180 g/cm3
Element: Lanthanum Z = 57.0 N = 138.9 A = 138.91 g/mole ElmMassFraction: 100.0 % ElmAbundance 100.0 %

Energy	PhotoElec	Compton	Conversion	PhotoElec	Compton	Conversion
100 keV	479.352 barn	24.6499 barn	0 pbarn	778.621 um	1.51413 cm	5.82593e+288 pc
200 keV	68.0279 barn	21.8212 barn	0 pbarn	5.48647 mm	1.71042 cm	5.82593e+288 pc
300 keV	22.0677 barn	19.5365 barn	0 pbarn	1.69131 cm	1.91044 cm	5.82593e+288 pc
400 keV	10.2117 barn	17.7867 barn	0 pbarn	3.65495 cm	2.09838 cm	5.82593e+288 pc
500 keV	5.77012 barn	16.3953 barn	0 pbarn	6.46861 cm	2.27646 cm	5.82593e+288 pc
600 keV	3.70134 barn	15.2535 barn	0 pbarn	10.0837 cm	2.44686 cm	5.82593e+288 pc
700 keV	2.58517 barn	14.294 barn	0 pbarn	14.4375 cm	2.61111 cm	5.82593e+288 pc
800 keV	1.91779 barn	13.4727 barn	0 pbarn	19.4616 cm	2.77028 cm	5.82593e+288 pc
900 keV	1.48768 barn	12.7594 barn	0 pbarn	25.0883 cm	2.92516 cm	5.82593e+288 pc
1000 keV	1.19421 barn	12.1325 barn	0 pbarn	31.2537 cm	3.07632 cm	5.82593e+288 pc
2 MeV	331.82 mbarn	8.38161 barn	753.882 mbarn	1.12481 m	4.453 cm	49.5082 cm
4 MeV	116.957 mbarn	5.46223 barn	2.79818 barn	3.19121 m	6.8329 8 cm	13.3384 cm
6 MeV	68.6994 mbarn	4.15924 barn	4.35632 barn	5.43284 m	8.9736 cm	8.56762 cm
8 MeV	48.2668 mbarn	3.39981 barn	5.56218 barn	7.73272 m	10.9781 cm	6.7102 cm
10 MeV	37.105 mbarn	2.89552 barn	6.53452 barn	10.0588 m	12.89 cm	5.71172 cm
12 MeV	30.102 mbarn	2.53327 barn	7.34396 barn	12.399 m	14.7332 cm	5.08218 cm
14 MeV	25.3083 mbarn	2.25896 barn	8.03415 barn	14.7475 m	16.5224 cm	4.64558 cm
16 MeV	21.8248 mbarn	2.04317 barn	8.63361 barn	17.1013 m	18.2673 cm	4.32303 cm
18 MeV	19.1806 mbarn	1.86849 barn	9.16189 barn	19.4589 m	19.9752 cm	4.07376 cm
20 MeV	17.1058 mbarn	1.72385 barn	9.63297 barn	21.8191 m	21.6512 cm	3.87454 cm
22 MeV	15.4349 mbarn	1.6019 barn	10.0571 barn	24.1811 m	23.2994 cm	3.71114 cm
24 MeV	14.0606 mbarn	1.49754 barn	10.4421 barn	26.5447 m	24.9232 cm	3.5743 cm
26 MeV	12.9105 mbarn	1.4071 barn	10.7941 barn	28.9094 m	26.525 cm	3.45776 cm
28 MeV	11.9339 mbarn	1.3279 barn	11.1177 barn	31.275 m	28.107 cm	3.35712 cm
30 MeV	11.0945 mbarn	1.2579 barn	11.4168 barn	33.6413 m	29.6711 cm	3.26917 cm
32 MeV	10.3652 mbarn	1.19554 barn	11.6945 barn	36.0082 m	31.2187 cm	3.19153 cm
34 MeV	9.7258 mbarn	1.1396 barn	11.9534 barn	38.3756 m	32.7512 cm	3.1224 cm
36 MeV	9.16059 mbarn	1.0891 barn	12.1957 barn	40.7434 m	34.2698 cm	3.06037 cm
38 MeV	8.65739 mbarn	1.04327 barn	12.4231 barn	43.1115 m	35.7753 cm	3.00436 cm
40 MeV	8.20654 mbarn	1.00147 barn	12.6372 barn	45.48 m	37.2687 cm	2.95346 cm

Table A.1: Cross section (columns 2-4) and mean free path (columns 5-7) associated to the photo-electric effect, Compton scattering and pair conversion for incident photons of various energies (column 1) in La material.

Material: Bromine density: 3.100 g/cm3
Element: Bromine ( ) Z = 35.0 N = 79.9 A = 79.90 g/mole ElmMassFraction: 100.0 % ElmAbundance 100.0 %

Energy	PhotoElec	Compton	Conversion	PhotoElec	Compton	Conversion
100 keV	68.0493 barn	15.8447 barn	0 pbarn	6.28974 mm	2.70129 cm	5.82593e+288 pc
200 keV	8.46567 barn	13.6608 barn	0 pbarn	5.05586 cm	3.13313 cm	5.82593e+288 pc
300 keV	2.55748 barn	12.1195 barn	0 pbarn	16.7357 cm	3.53159 cm	5.82593e+288 pc
400 keV	1.13634 barn	10.9864 barn	0 pbarn	37.6659 cm	3.89584 cm	5.82593e+288 pc
500 keV	631.083 mbarn	10.1027 barn	0 pbarn	67.8261 cm	4.23663 cm	5.82593e+288 pc
600 keV	402.323 mbarn	9.38529 barn	0 pbarn	1.06385 m	4.56046 cm	5.82593e+288 pc
700 keV	279.883 mbarn	8.78644 barn	0 pbarn	1.52925 m	4.87128 cm	5.82593e+288 pc
800 keV	207.149 mbarn	8.27611 barn	0 pbarn	2.0662 m	5.17166 cm	5.82593e+288 pc
900 keV	160.521 mbarn	7.83423 barn	0 pbarn	2.6664 m	5.46336 cm	5.82593e+288 pc
1000 keV	128.84 mbarn	7.44669 barn	0 pbarn	3.32206 m	5.74768 cm	5.82593e+288 pc
2 MeV	36.4286 mbarn	5.13894 barn	245.592 mbarn	11.7494 m	8.3288 cm	1.74278 m
4 MeV	13.2883 mbarn	3.34885 barn	1.03431 barn	32.2097 m	12.7809 cm	41.3814 cm
6 MeV	7.95647 mbarn	2.55033 barn	1.66443 barn	53.7942 m	16.7826 cm	25.7152 cm
8 MeV	5.65521 mbarn	2.08492 barn	2.15889 barn	75.6846 m	20.5289 cm	19.8255 cm
10 MeV	4.38097 mbarn	1.77584 barn	2.5603 barn	97.698 m	24.102 cm	16.7173 cm
12 MeV	3.57355 mbarn	1.55379 barn	2.89579 barn	119.772 m	27.5463 cm	14.7805 cm
14 MeV	3.0167 mbarn	1.38563 barn	3.18261 barn	141.881 m	30.8893 cm	13.4485 cm
16 MeV	2.60965 mbarn	1.25334 barn	3.43217 barn	164.011 m	34.1496 cm	12.4706 cm
18 MeV	2.29922 mbarn	1.14624 barn	3.65241 barn	186.155 m	37.3405 cm	11.7186 cm
20 MeV	2.0547 mbarn	1.05756 barn	3.849 barn	208.309 m	40.4718 cm	11.1201 cm
22 MeV	1.85712 mbarn	982.781 mbarn	4.02615 barn	230.47 m	43.5511 cm	10.6308 cm
24 MeV	1.69418 mbarn	918.785 mbarn	4.18706 barn	252.637 m	46.5846 cm	10.2223 cm
26 MeV	1.5575 mbarn	863.328 mbarn	4.33422 barn	274.807 m	49.577 cm	9.8752 cm
28 MeV	1.44121 mbarn	814.757 mbarn	4.46959 barn	296.981 m	52.5325 cm	9.5761 cm
30 MeV	1.34107 mbarn	771.828 mbarn	4.59476 barn	319.157 m	55.4544 cm	9.31524 cm
32 MeV	1.25394 mbarn	733.582 mbarn	4.71101 barn	341.335 m	58.3455 cm	9.08536 cm
34 MeV	1.17743 mbarn	699.271 mbarn	4.81942 barn	363.515 m	61.2083 cm	8.88099 cm
36 MeV	1.10971 mbarn	668.299 mbarn	4.92088 barn	385.696 m	64.045 cm	8.69788 cm
38 MeV	1.04936 mbarn	640.188 mbarn	5.01613 barn	407.878 m	66.8573 cm	8.53272 cm
40 MeV	995.235 mubarn	614.546 mbarn	5.10581 barn	430.061 m	69.6469 cm	8.38284 cm

Table A.2: Identical to Table A.1 for Br material.